Journal of The Electrochemical Society

OPEN ACCESS

Challenges of Predicting Temperature Dependent Capacity Loss Using the Example of NMC-LMO Lithium-Ion Battery Cells

To cite this article: L. Cloos *et al* 2024 *J. Electrochem. Soc.* **171** 040538

Journal of The Electrochemical Society, 2024 **171** 040538

Challenges of Predicting Temperature Dependent Capacity Loss Using the Example of NMC-LMO Lithium-Ion Battery Cells

L. Cloos,[1,z] J. Langer,[1] M. Schiffler,[2] A. Weber,[2] and Th. Wetzel[1]

[1]*Institute of Thermal Process Engineering (TVT), Karlsruhe Institute of Technology (KIT) Kaiserstraße 12, 76131 Karlsruhe, Germany*
[2]*Institute for Applied Materials - Electrochemical Technologies (IAM-ET), Karlsruhe Institute of Technology (KIT) Kaiserstraße 12, 76131 Karlsruhe, Germany*

In semi-empirical aging modeling of lithium ion-batteries an Arrhenius approach is commonly applied to describe the temperature dependency of a linear capacity loss. However, this dependency can change with degradation modes which was also observed in this cyclic aging study on NMC111-LMO graphite pouch cells in a temperature range of 4 °C to 48 °C. By means of differential voltage analysis and post-mortem analysis we correlated different regimes in capacity loss to degradation modes and aging mechanisms. In the first regime, a power dependency of time was observed. A second accelerated linear regime which followed an increase in loss of active material of the positive electrode was seen for medium (∼19 °C to 25 °C) to high aging temperatures. Transition metal dissolution was suggested to cause accelerated SEI growth. An activation energy could be estimated to 0.83 eV (± 0.17 eV, 95% CI). Finally, at aging temperatures around 45 °C we propose decreased charge transfer kinetics to result in mossy dendrites on the negative electrode which cause a final knee in aging trajectory. The findings highlight the necessity of sufficient aging temperatures and testing time.
 [DOI: 10.1149/1945-7111/ad3ec3]

Manuscript submitted February 16, 2024; revised manuscript received April 8, 2024. Published April 25, 2024.

Correctly estimating the lifetime of lithium-ion batteries is important to ensure the warranty of electric vehicles which range from 8 to 10 years and 100 to 155 thousand miles.[1] Many models to predict the lifetime are dependent on data fitting.[2] Semi-empirical aging models have a high applicability and simplicity when it comes to lithium-ion battery lifetime prediction.[2] In comparison to purely empirical models to describe capacity fade over time or charge-throughput they include physics-informed aspects.[3]

Many stress factors of cyclic aging[4] can be included in such a model. Even when keeping the stress factors constant the capacity fade dependency on time or charge throughput can show three different trajectories – accelerating, linear and decelerating.[5,6] To describe a decelerating trajectory, a root-square dependency was commonly used to account for diffusion limited steady-state growth[7] and Solid Electrolyte Interface (SEI) growth[8] which was especially applied for calendaric aging.[3,9] However, Attia et al.[10] have pointed out that SEI growth is not always diffusion limited. A transition over the different potencies of time from 1 over 0.5 to 0, which vary from reaction to diffusion and migration limitation of the SEI, were coupled by Kolzenberg et al.[11] Cyclic aging data can follow a power law of less than 0.5.[10,12] In other cyclic aging studies a linear dependency of the charge throughput has been found.[9,13,14] Kolzenberg et al.[15] correlated a transition from square-root to linear dependency during cyclic aging to decreased self-repairing of the SEI. These models mostly neglected the appearance of sudden deaths.[14] This seems adequate as the sudden death usually happens after reaching a remaining capacity of 80%[14,16] which is defined as End of Life (EoL) by USABC test procedures.[17]

An important stress factor on cyclic aging is temperature.[18,19] To account for the temperature influence on capacity loss during aging, the Arrhenius relation (1)[20] was proposed to model the temperature dependency of SEI growth,[21] including the activation energy E_A, Boltzmann-constant k_B and temperature T.

$$r = A \cdot \exp\left(-\frac{E_A}{k_B \cdot T}\right) \quad [1]$$

This relation was also found for the temperature dependency of cyclic aging.[8,22] In this case, a second temperature regime that is governed by a different aging mechanism was found.[13] Therefore, a double exponential form is used to describe both increased SEI growth and manganese dissolution at higher temperatures and lithium plating at lower temperatures on the example of an NMC/LMO blend positive electrode.[18] This dependency was also applied to other systems.[19,23,24] For this approach, a linearization of the aging rate is assumed.[18] However, many factors such as the C-Rate,[23,25,26] electrode thickness or energy density[23,25,26] and the cell chemistry[27] impact the dominant aging mechanism, which then dictates the temperature dependency.[25–27] Furthermore, the dominant aging mechanism can change over the lifetime.[28,29] For non-linear capacity fade Kucinskis et al.[25] have proposed linearization of certain State of Health (SoH) regions, which can be visualized in a 2D aging color map.[30] However, this approach is a step-wise solution, which does not take into account the underlying aging mechanisms. Therefore, the question as to how the temperature dependency of different aging trajectories correlates to the underlying aging mechanisms needs to be discussed. To answer this question a cyclic aging study on a pouch cell at different aging temperatures, Differential Voltage Analysis (DVA)[31] and post-mortem analysis were conducted in this study.

Experimental

The investigation was performed on a 20 Ah pouch cell with counter-tab configuration (SPB58253172P2, Enertech Internation, Inc.). It consists of NMC111-LMO positive electrode and graphite negative electrode which was confirmed via XRD measurements (D8 Advance diffractometer, Bruker). The cell with its dimensions 253 mm × 172 mm × 5.8 mm and weight of approximately 465 g has 18 positive electrode (PE) sheets and 17 negative negative (NE) electrode sheets. The nominal voltage is 3.75 V.

Test setup, cycling and regular reference tests.—The cells were cycled with a BaSyTec XCTS (BaSyTec GmbH) in a controlled thermal environment. More precisely, each cell was clamped between aluminum plates with fluid channels on each side of the pouch cell. Water was used as coolant which was supplied by thermostats and cryostats depending on the temperature level (ECO 4 S for 19 °C, 40 °C, 45 °C and 48 °C; RE1050S for 25 °C; VARIOCOOL 2000 for 4 °C (LAUDA Dr R. WOBSER GMBH & CO. KG)). This setup allowed individual temperature boundary

[z]E-mail: lisa.cloos@kit.edu

Table I. Tested cells cell names and measured mean surface temperatures during cycling (T_{EAT}) and regular reference test (RTP) test batch.

Cell name	T_{EAT}/ °C	Test batch
4 °C ***a***	3.6	1
4 °C ***b***	4.5	2
19 °C ***a***	19.0	2
25 °C ***a***	25.5	1
25 °C ***b***	25.6	1
40 °C ***a***	40.5	2
45 °C ***a***	45.2	1
48 °C ***a***	48.1	2

conditions between 4 °C and 48 °C. The cell names are listed accordingly in Table I. Additional cells at the same temperature test condition are labeled "b". The temperature was controlled via thermocouples type K (ES Electronic Sensor GmbH) placed on the surface of each pouch cell. The entire temperature measurement path was calibrated previous to the aging study with a setup of OCEANUS-6 series, milliK precision thermometer and a PT-25 reference thermometer (Isothermal Technology Limited). The equivalent aging temperature T_{EAT}[19] is given in Table I as the actual mean surface temperature during cycling over the entire cyclic aging study. The internal temperature of such a pouch cell could vary up to 1 K trough-plane.[32] To mitigate the influence of the thermocouple, a 1 mm gap filler was placed between the pouch cell and the aluminum plate (TGF-V-Si, HALA Conec GmbH & Co. KG). The aluminum plates also ensured a constant pressure of 0.5 bar, which was applied via springs. All cells including the described setup were placed in a climate chamber at a constant ambient temperature of 25 °C.

Other cyclic aging stress-factors were kept constant. The cells were cycled with 2 C between the cut-off voltages of 3 V and 4.2 V without pauses. Regular Reference Tests (RTP) were performed at the nominal temperature of 25 °C. Thermal and electrical equilibration was ensured with voltage and temperature before conducting the RTP. First, a nominal capacity (C_N) measurement at C/2 and a quasi-Open Circuit Voltage (qOCV) at C/10 in discharge direction were measured. The start point to these measurements was reached with a CC-CV (C/2, C/40 cut-off) charge phase. Afterwards, 18 s pulses were conducted at various states of charge such as 50% with a C-Rate of 1 C in discharging direction. These RTPs were done with varying intervals between test batch one (4 °C *a*, 25 °C *a*, 25 °C *b*, 45 °C *a*) and two (4 °C *b*, 19 °C *a*, 40 °C *a*, 48 °C *a*). In the first test batch, RTPs were performed every 50 full cycles for the first 10 RTPs. Afterwards, the checkup was performed every 100 full cycles. Test batch two was checked upon every 100 full cycles from the beginning. Almost no difference between the capacity fades of cell 4 °C *a* and 4 °C *b* from the different batches can be seen in these first RTPs (Fig. 2). Therefore, we suggest that no impact of different RTP schedules for the test batches one and two on the capacity fade can be observed.

Experimental cell setup.—To analyze the degradation modes via DVA for both electrodes individually, experimental cell material was harvested from a new cell at Begin of Life (BoL) and after cycling at 45 °C until EoL. Here, the EoL is defined as the end of testing. Hence, the SoH of the cell aged at 45 °C at EoL was 67%. The cells were opened in a controlled inert argon atmosphere in a glove-box. The electrodes underwent a thorough preparation process involving their separation and triple washing with Dimethylcarbonate (DMC) to eliminate any residual conductive salt originating from the electrolyte. Additionally, the active material of the electrodes was delaminated from the current collector on one side through the utilization of N-methyl-2-pyrrolidone (NMP). Circular coins with a standardized diameter of 18 mm were punched out from the electrodes for further experimentation.

The experimental cell configuration encapsulated within a PAT-Cell housing (EL-CELL GmbH) was used for the electrical characterization of the electrodes. In the context of half-cell measurements, negative and positive electrode coins were individually assembled against lithium. For full-cell measurements, a cell with both negative and positive electrode was constructed. The electrode coins were isolated by an insulation sleeve (EL-CELL GmbH), comprising a polypropylene (PP) fiber/polyethylene (PE) membrane, alongside a lithium reference. The separator was soaked with 80 μl LP30 (1 M $LiPF_6$ EC/DMC) electrolyte.

Cycling of the experimental cells was executed utilizing a BaSyTec XCTS (BaSyTec GmbH) from 3 V to 4.3 V for the positive electrode half-cell (positive electrode vs lithium), 0.01 V to 1 V for the negative half-cell (negative electrode vs lithium) and 3 V to 4.2 V for the full cell (negative electrode vs positive electrode). The applied currents for cycling procedures were based on the calculated areal capacity derived from the cell's overall capacity and the aggregate area of the active material. The cyclic protocol included formation cycles before a cycle with C/100 was conducted.

Differential voltage analysis and further analysis methods.—To quantify the degradation modes via DVA,[31] the approach presented by Schmitt et al.[33] is used. They aligned half-cell DVA curves that can be measured at one point in time to the aged pouch cell DVA curves.[33] Afterwards, the degradation modes could be calculated based on the alignment factors,[33] which was done accordingly in this study. The half-cell measurements at BoL were used for this method. The minimization was performed with the *lsqnonlin* solver in MATLAB®. Contrary to the method described by Schmitt et al.[33] the voltage curves were used for alignment, which was also previously done by Hu et al.[34] Another difference to Schmitt et al.[33] is the cut-off at the sides of the voltage curves was increased from 1% to 5% to avoid optimization to the steep slopes.

As another quantification step, the capacity loss was analyzed for acceleration onsets and knees. A Bacon-Watts[35] model which was adapted by Fermín-Cueto et al.[36] to identify knee-points can be used for this purpose. Fermín-Cueto et al.[36] also proposed a double Bacon-Watts function to predict the knee onset. Similarly, we used this double Bacon-Watts function to identify an acceleration onset and the final knee. Again, the *lsqnonlin* solver in MATLAB® was utilized.

A further analysis on the capacity loss was performed. In a first step, we assumed the capacity loss to follow a power function as shown in Eq. 2 with r_{pow} and the exponent α as variables. To visualize the evolution of the exponent α over the course of aging, the power function was fitted over a sliding window of 20 days with the *fit* function using the non-linear least squares method in MATLAB®. In a second step, the identified changes in the aging trajectory from the double Bacon-Watts function[36] were used to separate the slopes in aging trajectory. Then, the power (pow) function and if applicable a linear (lin) function (3) was fitted using the *fit* function with non-linear least squares method in MATLAB®. The linear function consists of the axis intercept B and the slope r_{lin}.

$$\frac{C_N}{C_{N,BoL}} = 1 - r_{pow} \cdot X^{\alpha} \quad [2]$$

$$\frac{C_N}{C_{N,BoL}} = B - r_{lin} \cdot X$$
$$X = time\ or\ EFC \quad [3]$$

Post-mortem analysis.—The aged pouch cells were opened in the same manner as previously described for the experimental cell setup. For each temperature level—low, medium and high—a cell

was opened at the respective SoH (4 °C *a*: 85.9% SoH; 25 °C *b*: 85.8% SoH; 45 °C *a*: 67.0% SoH). Samples were cut from the electrodes and washed with DMC. Then, they were only exposed to the ambient atmosphere shortly before inserting them into microscopes. Both a digital light microscope (VHX 7000, Keyence Corporation) and a scanning electron microscope (SEM) (LEO 1530 Gemini) were used. For the latter, an acceleration voltage of 2 kV to 5 kV was applied for the SEM images. Energy dispersive X-ray spectroscopy (EDX) was performed with an acceleration voltage of 15 kV. Inductively coupled plasma optical emission spectroscopy (ICP-OES) was applied for the found depositions on the sample 45 °C *a*. The depositions were scraped off with a scalpel. The sample was dissolved in acid while traces of graphite, that stuck to the depositions, remained. The measurement was conducted with an iCAP 7000 (ThermoFisher Scientific).

Results and Discussion

The aim is to set up a physically meaningful semi-empirical temperature dependent aging model for the investigated NMC-LMO/Graphite pouch cell. Therefore, the trajectories of the temperature dependent capacity fade and resistance increase during cyclic aging will be discussed in a first step. As the temperature dependency of the aging behavior is linked to the dominant aging mechanism,[25–27] degradation modes will be analyzed for both experimental cell setup as well as for the pouch cells. Post-mortem analysis is used to provide even more detailed insights into the prevailing aging mechanisms. Lastly, correlations between capacity, degradation modes and aging mechanisms will be discussed and a new model will be proposed. An overview of the procedure is given in Fig. 1.

Capacity decrease and resistance increase.—The relative capacity loss is plotted over time in days in Fig. 2a. 100 days equal approximately 2250 equivalent full cycles (EFC). The EFCs are calculated with the cumulative charge throughput from both charge and discharge of each cycle divided by the cumulative charge throughput of the first C/2 cycle performed at the initial RTP at nominal conditions. The different aging temperature levels are indicated with different colors (blue–4 °C, light blue–19 °C, green–25 °C, yellow–40 °C, magenta–45 °C, dark magenta–48 °C). Additional cells for one temperature test condition ("b") are depicted with dashed lines. Figure 2b provides a zoom into the SoH range from 90% to 100% of Fig. 2a. In this figure, a closer look at the cells 25 °C *a* and 25 °C *b* reveal an almost indistinguishable capacity fade, which indicates good reproducibility. The cells aged at around 4 °C show increasing deviation after approximately 15 days, which could be due to the slight difference in average temperature over cycling of around 1 K. This temperature increase could not be correlated to an increase in resistance (Fig. 2c) and is therefore likely due to the experimental setup.

An initial capacity drop can be seen for all investigated cells in Fig. 2b. In the first 13 days the capacity decrease trajectories are strongly overlapping and decelerating for all temperature boundary conditions. For the aging temperatures below 25 °C (4 °C, 19 °C), the decelerating aging trajectory continues, while the medium to higher aging temperatures (25 °C, 40 °C, 45 °C and 48 °C) lead to an acceleration in the aging trajectory at different EFCs. Few data points in the capacity loss for the aging temperature of 19 °C also hint towards an acceleration. This start of accelerated aging occurs well above a SoH of 90%. With increasing aging temperature, the acceleration occurs at a lower EFC. The aging trajectories then change to a linear aging trajectory whose slope increases with increasing aging temperature (25 °C < 40 °C < 45 °C < 48 °C). This also means, that the lower aging temperatures (4 °C, 19 °C) with the ongoing mostly decelerating trend show less relative capacity fade in the long run. The least relative capacity fade at approximately ∼90 days is observed for an aging temperature of 19 °C. Only for the high aging temperatures (45 °C and 48 °C) a final knee can be seen below 80% SoH.

The relative 18 s pulse resistance increase is shown in Fig. 2c. Similarly to the capacity loss, an acceleration of the resistance increase can be seen for medium to high aging temperatures. However, this acceleration seems to occur at a later point in time, which can clearly be seen for the high aging temperatures. The capacity loss only becomes sensitive to resistance increase if the discharge ends in the flat region of the voltage curve,[6] which is not the case here. Therefore, the capacity loss acceleration is unlikely to be due to the resistance increase. Even though resistances do not necessarily cause a capacity knee,[6] a strong linear relation between resistance elbows and capacity knees were seen.[37]

In comparison with literature, NMC-LMO/Graphite cells usually have a decelerating[38–41] or linear capacity loss behavior.[42] Only in one investigation for the same cell chemistry at 25 °C an acceleration of the aging trajectory in the region of 95% SoH was seen.[18] Dubarry et al.[17] have discussed such an acceleration between a SoH of 80% to 90% in a study on the same cell chemistry. They have found an increase in Loss of Active Material of the positive electrode (LAM_{PE}).[17] Assuming similar mechanisms resulting in a knee[6] also causing this acceleration an increase of one dominant degradation mode[43,44] or a change in dominating degradation mode[28,29] are possible. To get a general idea about dominating degradation mode for the investigated cell DVA is an adequate tool.

Differential voltage analysis on half-cells and full-cells.—With half-cell measurements of positive and negative electrodes LAM can be easily seen. LAM results in a contraction of the voltage curves.[31] Loss of Lithium Inventory (LLI)[45] causes a shift between positive electrode and negative electrode curve, which can be seen in full-cell configuration.[31] The cell 45 °C *a* is chosen as an example for high capacity loss. DVA graphs of the positive and negative electrode DVAs with respective half-cell and full-cell measurement at EoL are shown in Figs. 3a–3d. The balancing of positive and negative half-cell electrode DVA to the pouch cell DVA[31] is shown in Fig. 3a.

The NMC-LMO blend positive electrode has two minima in all presented measurements (Fig. 3c). The one at higher potentials can be assigned to LMO and the one at lower potentials to NMC.[41] The positive electrode capacity contracts by about 19%, which is a significant amount of LAM_{PE}. No clear trend can be seen of a NMC and LMO peak shift. The negative electrode shows two very different trends in the half-cell and full-cell measurement. The

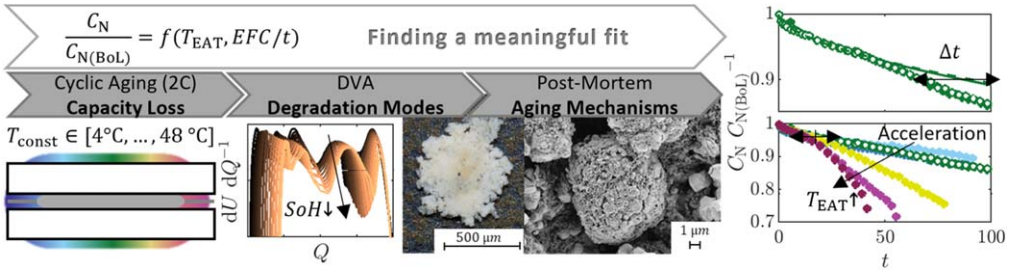

Figure 1. Overview of the procedure in this publication to find a semi-empirical model for temperature dependent cyclic aging.

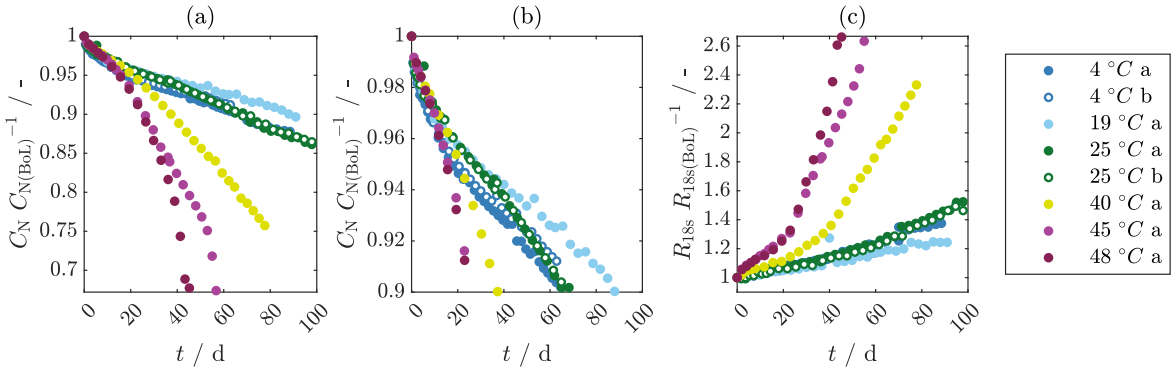

Figure 2. Cyclic aging study at different aging temperature levels (blue–4 °C, light blue–19 °C, green–25 °C, yellow–40 °C, magenta–45 °C, dark magenta–48 °C). Additional cells for one temperature test condition ("b") are depicted with unfilled markers. (a) Relative capacity loss over time in days; (b) Zoom into relative capacity loss over time in days; (c) Relative 18 s pulse resistance increase at 50% state of charge over time in days. (100 days ≈ 2250 equivalent full cycles (EFC)).

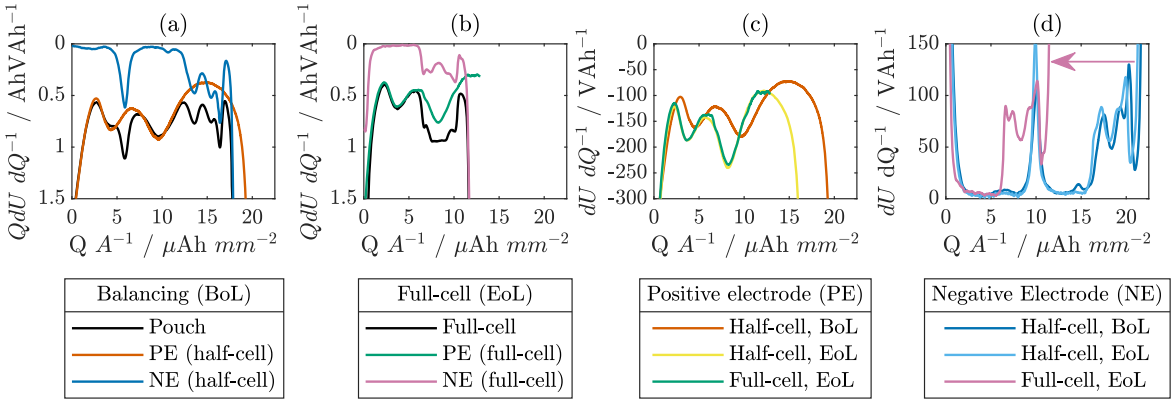

Figure 3. (a) Balancing of half-cell negative (NE) and positive (PE) electrode to pouch cell DVA at Begin of Life (BoL); (b) Full-cell DVA with respective negative and positive electrode DVA in full-cell configuration at End of Life (EoL) of cell 45 °C *a*; (c) Positive electrode DVA at BoL and EoL for half-cell and full-cell configuration of cell 45 °C *a*; (d) Negative electrode DVA at BoL and EoL half-cell and full-cell configuration of cell 45 °C *a*; The arrow indicates the shift of the negative half-cell to full-cell DVA at EoL. (black–pouch and full-cell, orange–half-cell PE BoL, yellow–half-cell PE BoL, green–full-cell PE EoL, blue–half-cell NE BoL, light blue–half-cell NE EoL, pink–full-cell NE EoL).

half-cell DVA of the negative electrode does not change drastically in comparison to BoL. All graphite peaks are still visible. The contraction is around 2%. This is not true for the negative electrode DVA calculated from full-cell measurements at EoL. Here, the contraction is significant of around 47%. This means, that LAM_{NE} is minor. Any losses in active lithium were compensated by the lithium metal counter electrode. The large difference between the half-cell and full-cell measurement of the negative electrode at EoL indicate a large LLI. A similar difference between the setups were seen by Sieg et al.[46]

Differential voltage analysis on pouch cells.—While these half-cell measurements only give a momentary insight into the degradation modes at BoL and EoL, a DVA at each RTP can show the degradation mode trends over cyclic aging. In Figs. 4a–4c) the estimated LLI, LAM_{PE} and LAM_{NE} for the described method in "Differential Voltage Analysis and Further Analysis Methods" section is shown. The squared norm of the residuals of the method is presented in Fig. 4e. For comparison, the capacity loss is also plotted in Fig. 4d. In this figure, the described onsets of acceleration and knees in capacity loss were quantified with the double Bacon-Watts[36] model from "Differential Voltage Analysis and Further Analysis Methods" section. The onset of acceleration of the capacity loss is marked with a dotted vertical line and the final knee is marked with a vertical dot dash line.

The trajectories in LLI appear like the inverse of the capacity loss, including the acceleration. An acceleration can also be seen in LAM_{PE}. However, this acceleration starts slightly earlier. Here, both the low aging temperatures (3 °C and 19 °C) show the least increase. Generally, LAM_{PE} is quantitatively less than LLI. As already predicted by the half-cell measurements LAM_{NE} is very low for all investigated aging temperatures. Interestingly, LAM_{NE} increases significantly at the same time of the capacity loss knee. It needs to be taken into account that the squared norm of the residuals increases with decreasing SoH.

DVA of half- and full-cells and pouch cells suggested LLI to be the dominant degradation mode. For NMC-LMO cells, LLI was previously found to be the dominant degradation mode at an ambient temperature and above SoH 80%.[17,47] Two regimes that were already identified for the capacity loss could also be identified in quantitative DVA; being an increase in LAM_{PE} followed by an increase in LLI. Dubarry et al.[17] related an increase of LAM_{PE} to the capacity loss acceleration for an NMC111-LMO cell at room temperature. They proposed that LLI in the first regime leads to grain isolation and/or pore clogging of active material and LAM.[17] Regarding these results, it seems more likely that the aging mechanism causing an increase in LAM_{PE} accelerates and then triggers an acceleration in LLI. Furthermore, the results suggest an increase in LAM_{NE} to correlate to the final knee in capacity loss. Post-mortem analysis could give further evidence as to which aging mechanisms are causing this behavior.

Post-mortem analysis.—The post-mortem analysis which is discussed in this section consisted of a visual inspection and SEM analysis. Cells from three different aging temperature levels which showed different aging trajectories were chosen. The low

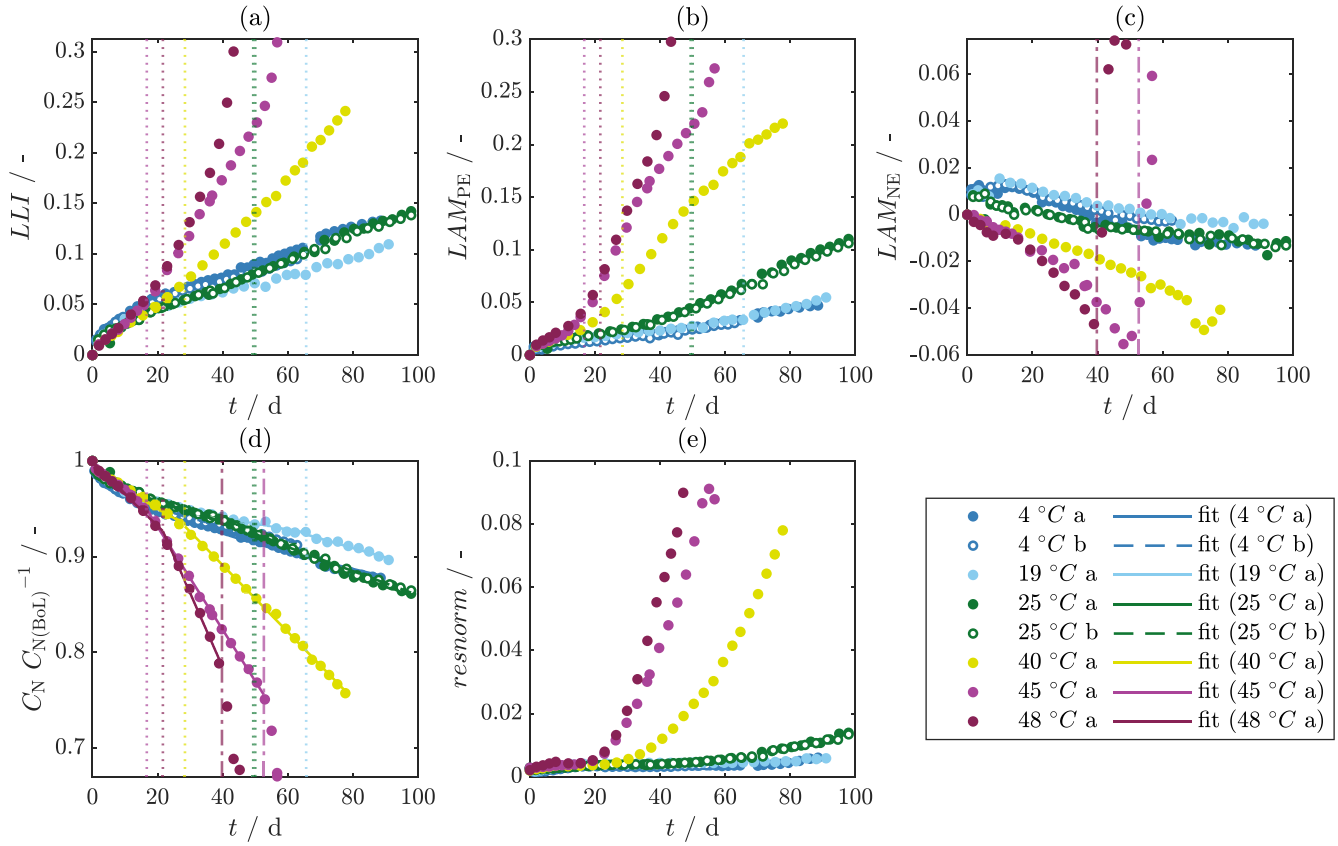

Figure 4. Quantitative analysis of degradation modes of the cyclic aging study at different aging temperature levels (blue–4 °C, light blue–19 °C, green–25 °C, yellow–40 °C, magenta–45 °C, dark magenta–48 °C). Additional cells for one temperature test condition ("b") are depicted with unfilled markers or dashed lines. The identified onset of capacity loss acceleration is indicated with vertical dotted lines and the identified knees with vertical dot dash lines in the respective color. (a) Loss of lithium inventory (LLI) over time in days; (b) Loss of active material of the positive electrode (LAM_{PE}) over time in days; (c) Loss of active material of the negative electrode (LAM_{NE}) over time in days; (d) Relative capacity loss over time in days, the fitted aging function is shown with lines; (e) Squared norm of the residuals of the quantitative DVA. (100 days ≈ 2250 equivalent full cycles (EFC)).

temperature level was represented by the cell aged at 4 °C, the medium temperature level at 25 °C and the high temperature level at 45 °C respectively. Upon cell opening, the electrode sheets of cell aged at 4 °C had a liquid film on the sheets in the moment of disassembly. The other cells at a higher aging temperature level showed a fine layer on the electrodes after cell opening which resembled a frost pattern. This could be washed off with DMC. Also, the negative electrode sheets themselves displayed visual differences while the positive electrode sheets were macroscopically unchanged. The negative electrode sheets of the cell aged at 4 °C had white depositions at the edges. The cell aged at 45 °C also had white circular depositions in the center and close to the current collectors (Fig. 5a).

Light microscopy of the white depositions of the cell aged at 45 °C (Fig. 5b) revealed a pillar-like structure with yellowish discoloration in the center. SEM pictures showed a different structure towards the center (Fig. 5c) and towards the edges (Fig. 5d) of the white deposition. At the edges, a mossy structure can be seen, whereas the center seems to be covered with an uneven layer. SEM images of the white depositions on the 4 °C *a* cell revealed a similar structure as described for the depositions of the 45 °C *a* cell although less in height. ICP-OES measurements of the scraped of white depositions on the 45 °C *a* cell had the largest measurable content to be Lithium. Manganese, Nickel and Cobalt were present in small contents. SEM-EDX on the depositions showed prominent peaks of Oxygen, Phosphorous and Fluorine.

For the low temperature aging (4 °C) lithium plating at the edges can be expected due to the edge effect.[48,49] Also, at high temperature aging (45 °C) ICP-OES confirmed the presence of lithium in the white pillar like depositions. Even though lithium plating at higher temperatures is not expected[18] it can occur when inhomogeneities are present.[50,51] Storch et al.[50] proposed an interplay between temperature, current density and lithium concentration gradient to cause local lithium plating in their large format cells. The local current density is also critical to the lithium growth mechanisms.[52] The interaction between local current density, lithium concentration and fractured SEI enables mossy dendrites even under normal charge scenarios[53] whose shape resemble the found depositions on the negative electrodes at an aging temperature of 45 °C (Fig. 5b). The layer on top of the pillars, which can be seen in Fig. 5b resembles the layer found by Paarmann et al.[54] They suggested this to be a type of lithium plating.[54] The deposited lithium can become inactive "dead-lithium".[55] This could explain the lack of metallic sheen of the depositions.

Apart from the observed depositions SEM also reveals differences in the electrode particles between the cells aged at different temperatures. To illustrate these differences both negative electrode and positive electrode SEM at BoL and EoL of the three different temperature levels are selected as representation in Fig. 6. At BoL, the large round particles in the positive electrode blend can be identified as NMC and the smaller square shaped particles as LMO.[56] When comparing the positive electrode at BoL and at EoL of the cell 25 °C *a*, a surface layer has formed on top of a large NMC particle, which looks different to carbon black binder phase at BoL (Figs. 6a and 6b). This surface layer can be seen on many positive electrode particles for all investigated aging temperature levels. In case of the 4 °C *a* cell a close up of one of these layers which peeled off was taken (Fig. 6 (d)). Here, the layer thickness can be estimated to about 200 nm. At an aging temperature of 45 °C, not only the surface layer can be seen but also particles seem to be

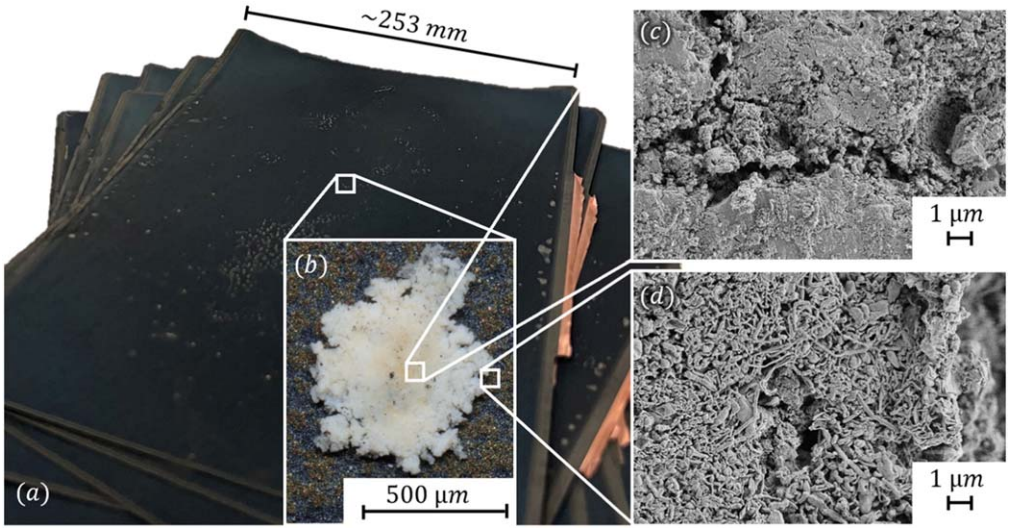

Figure 5. Picture of the negative electrode sheets (a), light microscopy (b) and SEM pictures (c), (d) of a white deposition at EoL of cell 45 °C *a*.

ground to fine powder in some areas (Fig. 6c). Generally, particle cracking can be observed in all probes but also at BoL. Therefore, there is no clear trend.

A known aging mechanism on the positive electrode is the formation of a Cathode Electrolyte Interface (CEI). However, CEI is known to be couple of nm thick,[57] which is well below the estimated layer thickness of 200 nm of the observed layer in this investigation. Only at high voltages above 4.5 V, a higher thickness around 2 μm layer on NMC111 particles was seen.[58] Another aging mechanism at high voltages for NMC particles is particle pulverization,[59] which was observed for a high aging temperature of 45 °C (Fig. 6c). In this investigation, high cut-off voltages were avoided. The maximum positive electrode voltage was 4.27 V vs Li/Li^+ at BoL. This is low even when taking into account that the onset potential for aging mechanisms such as oxygen release decreases with increasing temperature due to lower overpotentials.[60] Darma et al.[61] argued, that already at 4.05 V NMC was stressed mechanically in their NMC-LMO-NCA blend material. In the following analysis, Lang et al.[62] found microcracks in the NMC. Cracking is known to be a critical mechanism for layer-structure positive electrodes at high voltages.[63] Lang et al.[62] argued this to become a self-enforcing trend. This mechanism could explain both layer formation on positive electrode particles and positive electrode particle pulverization at higher temperatures such as 45 °C. In an NMC-LMO blend material Dubarry et al.[64] have seen over-lithiation of LMO due to differences in the kinetics of the blend which should not appear under normal cycling conditions.

Whereas layer formation on the positive electrode particles was observed for all aging temperature levels layer formation on the negative electrodes was noticed to various extents. In comparison to BoL, the negative electrode of the 25 °C *a* at EoL shows rounding of the edges which can be consequence of surface layer formation (Figs. 6e and 6f). This is also true for the negative electrodes of the 45 °C *a* (Fig. 6g). For the cell aged at 4 °C the rounding of negative electrode particles is not as visible.

A common aging mechanism of the negative electrode is the SEI.[65] Blurring of the graphite edges is usually associated with SEI.[54] The SEM pictures suggest that the SEI layer increases at higher aging temperatures of 25 °C and above, which is likely to be due to the described positive electrode aging mechanisms. At higher temperatures such as 55 °C, Mn dissolution in $LiPF_6$ electrolytes occurs.[66] This aging mechanism of metal dissolution is known for both spinel LMO and layered oxide NMC.[67] The dissolved manganese ions can then interact with the SEI and enhance the formation of inactive species.[68,69] Also, in this study, ICP-OES measurements of the depositions on the negative electrode at an aging temperature of 45 °C revealed the presence of transition metals. These side reactions can also cause Li salt and electrolyte depletion[41,70] which is in line with decreased wetting of electrode sheets upon cell disassembly.[71] Transition metal dissolution is not only triggered by higher temperatures but also higher voltages[72] which also seems to be an issue here.

These aging mechanisms can be correlated to the features found in capacity loss, resistance increase and DVA. The post-mortem results suggest that over-lithiation is an issue for this blend positive electrode. High voltage operation of a positive electrode can cause layer formation,[58] particle cracking[63] and transition metal dissolution.[72] Layer formation on the positive electrode did not necessarily lead to LAM_{PE}, which can be seen on the basis of an aging temperature of 4 °C. Positive electrode surface layers are not known to passivate.[14,73] At medium to higher aging temperatures the processes on the positive electrode seem to accelerate, which is then followed by an increase in LLI and decrease in capacity loss. Transition metal dissolution is a known process to increase SEI layer formation.[68] The insertion of manganese species in the SEI alters the SEI[69,74] and increases the charge-transfer impedance.[75] An increase in the pulse resistance could be observed. Decreased charge-transfer causing plating is considered a threshold knee trajectory.[6,16] Due to the changed SEI, we suggest an easier onset for mossy dendrites as they grow due to a fractured SEI.[53] This knee coincides with an increase in LAM_{NE}. Another aging mechanism that can be correlated with this final knee is particle pulverization, which is the worst case of particle cracking.

Consequences for temperature dependent semi-empirical aging model.—To describe the aging trajectories for the investigated cell an assumption of a linear aging trend whose slope is often used to describe the temperature dependency in an Arrhenius fit[18] is not applicable. Not only did different aging temperatures lead to different aging trajectories which was already found by Kucinskis et al.[25] but also changes in the aging trajectories were observed. Clearly, different aging modeling are necessary. For this modeling the final knee below a SoH of 80% is excluded.

To analyze the changes in the capacity loss a power function (2) was fitted over a sliding window as described in "Differential Voltage Analysis and Further Analysis Methods" section. The exponent α is presented in Fig. 7a over the course of aging with the 95% confidence interval (CI) as a shaded area in the respective color. Changes in the exponent can indicate changed limitation with increasing SEI thickness; from reaction to diffusion to electron

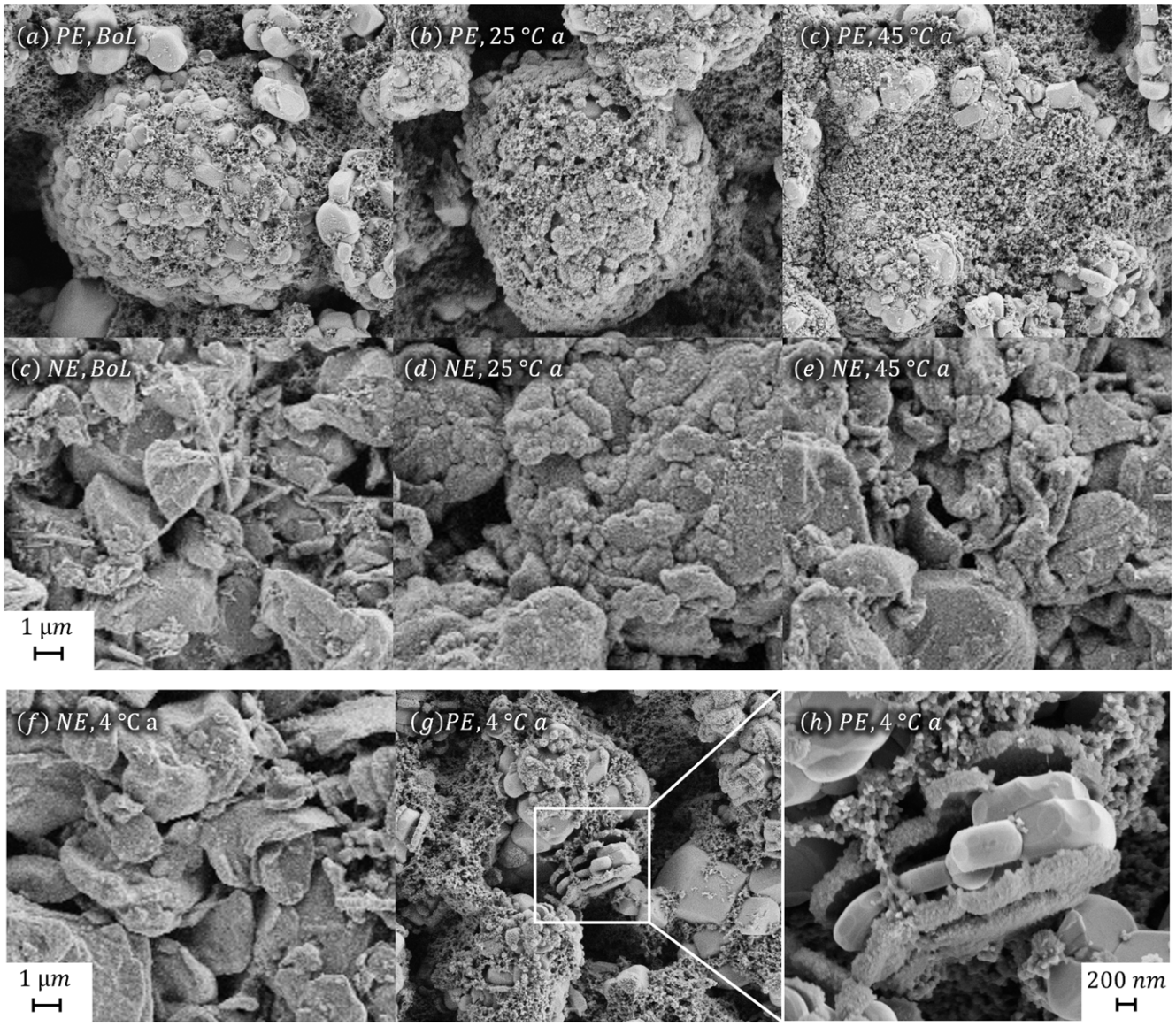

Figure 6. SEM pictures of positive electrode (PE) (a), (b), (c), (g), (h) and negative electrodes (NE) (c)–(f) at Begin of Life (BoL) (a), (c) and End of Life (EoL) for cells aged at temperatures of 25 °C *b* (b), (d), 45 °C *a* (c), (e) and 4 °C *a* (f)–(h).

migration limitation.[11] Even though the confidence intervals are wide, trends for aging temperatures below and above 25 °C can be differentiated. While the exponent α at aging temperatures of 25 °C firstly lies around 0.5 higher aging temperatures result in an exponent of 0.7 to 1. The exponents of the medium aging temperatures all start to increase at some point in time while the exponents at higher aging temperatures increase from the beginning. The increase of the exponent at low to medium aging temperatures of 3 °C and 19 °C is unclear due to high confidence intervals. Exponents well above one can be correlated to the beginning of the knee.

Relating these results to the investigation of SEI growth regimes of Kolzenberg et al.[11,15] we observed the transition from self-passivation ($\alpha = 0.5$) to non-passivation ($\alpha = 1$) SEI growth for medium aging temperatures (∼19 °C, 25 °C). Either at higher aging temperatures this transition is too fast or another mechanism is at play. An exponent of 0.76 was previously found in an experimental study of Gilbert et al.[72] It describes a diffusion/percolation limited mechanism through the inner and outer SEI.[72,76] In their study for higher cut-off voltages, this initial regime with an exponent of 0.76 was swiftly followed by an intermediate linear regime[72] which marks a fast change in SEI growth regimes from lower to higher growth rate. Gilbert et al.[72] argue that the linearity is an artifact of multiple occurring processes during their cyclic aging experiments. This linear regime is controlled by cracking of positive electrode particles and loss of transition metal ions, which result in faster SEI growth rate than solely diffusion controlled growth.[72] This is in line with the findings of this study.

Generally, the investigated cell is rather insensitive to lower aging temperatures, which is entirely different to the results by Waldmann et al.[18] with the same cell chemistry. We observed only slight edge plating for aging temperatures of 3 °C. This highlights that not only the cell chemistry but also other design factors such as electrode thickness have an impact on the optimum aging temperature.[25,26] This could be related to the fact that the positive electrode chemistry and electrode material load has shown to shift the degradation modes.[77]

The analysis of the exponent α supports our findings regarding the two aging regimes. Therefore, we used the found acceleration onsets and knees from the double Bacon-Watts model as boundaries to fit a power function (2) to the first regime and a linear function (3) to the second regime as described in "Differential Voltage Analysis

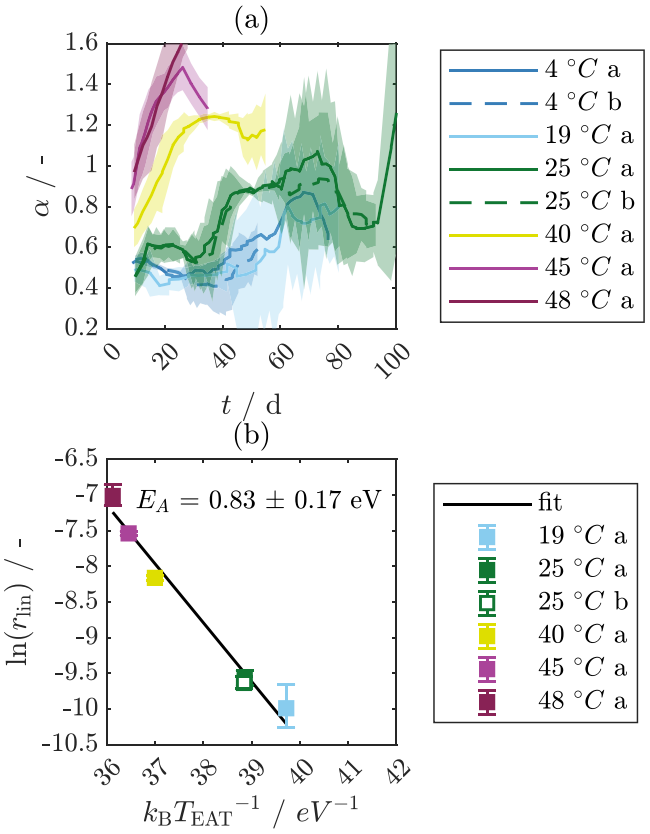

Figure 7. (a) Exponent α of the Eq. 2 fitted over a sliding window of 20 days of the capacity loss at different aging temperatures with the 95% confidence interval shown as shaded area (blue–4 °C, light blue–19 °C, green–25 °C, yellow–40 °C, magenta–45 °C, dark magenta–48 °C); (b) Arrhenius plot of the pre-factor r_{lin} of Eq. 3 fitted to the linear region of the capacity loss; The error bars mark 95% confidence interval of fitting factors. (black–Arrhenius fit with activation Energy (E_A)); Additional cells for one temperature test condition ("b") are depicted with unfilled markers or dashed lines.

and Further Analysis Methods" section. The results for the fittings are shown with continuous lines in Fig. 4d. The values for the parameters can be found in Table II. Due to multiple tested aging temperatures in this investigation an Arrhenius plot can be drawn for the slope r_{lin} of the linear regime over time (Fig. 7b). The error bars highlight the 95% CI which is higher for the aging temperature of 19 °C. This aging temperature only showed signs of acceleration. It reveals an estimate for the activation energy of 0.83 eV (± 0.17 eV, 95% CI) which is higher than the measured activation energies for cyclic aging in the high temperature regime. These range from 31.7 kJ mol^{-1} to 54.99 kJ mol^{-1}[18,22,78] in comparison to 80.08 kJ mol^{-1}. This means that the activation energy for the multiple previously described processes is higher than conventional SEI growth. It is also larger than the activation energy of Mn dissolution which was found by Waldmann et al.[79] via ICP-OES with 0.33 ± 0.02 eV.

Neglecting the different regions can have minor to very severe consequences on the aging prediction accuracy. Assuming a linear trend for example can describe the overall trend relatively well. However, it cannot describe the initial capacity loss especially for high and low temperatures. Even more important is the necessary testing time. If the testing time does not cover the accelerated regime an extrapolation is not possible. This is illustrated in Fig. 1 on the top right on the example of an aging temperature of 25 °C. A prediction based only on 50 days of testing would lead to a misjudgment of the achievable days for a SoH of 90% by about 20 days (30%).

Conclusions

Temperature dependent semi-empirical aging models are often described via an Arrhenius dependency. However, it has been shown that this dependency can change with the slope of the aging trajectory.[25] In this paper we set up a physically meaningful temperature dependent aging model for a NMC111-LMO graphite pouch cell. We did not only observe different aging trajectories for the different aging temperatures ranging from 4 °C to 48 °C but also an acceleration in aging trajectories over the lifetime for some aging temperatures. With means of DVA and post-mortem analysis a correlation between capacity loss, degradation modes and aging mechanisms could be derived:

-Lower aging temperatures (3 °C) mostly followed a $t^{0.5}$ behavior. A qualitatively similar behavior was observed for the LLI. The only visible aging mechanism apart from slight edge plating was layer formation on the positive electrode (∼200 nm) which could be due to over-lithiation of the blend positive electrode.[62,64]
-Medium aging temperatures (∼19 °C to 25 °C) first followed a $t^{0.5}$ behavior but then accelerated into a linear regime which was also seen for higher aging temperatures.
-High aging temperatures (40 °C to 48 °C) had a power dependency above 0.7 in the first regime before the acceleration into a linear regime. An increase in LAM_{PE} preceded an increase in LLI and the accelerated capacity loss. This acceleration is a known process at higher voltages where transition metal dissolution leads to diffusion/percolation controlled SEI growth.[72] The process accelerates due to further stress on the oxide particles which leads to a fast linear growth of SEI.[72] An increased layer formation on the negative electrode and transition metal dissolution could indeed be seen. The activation energy of these processes could be estimated to 0.83 eV (± 0.17 eV, 95% CI). Finally, we suggest the increased charge transfer resistance of the SEI to enable mossy dendrite lithium growth which results in a final knee and coincides with an increase in LAM_{NE}.

This study clearly shows that sufficient testing both in aging temperatures as well as testing time is needed to depict all aging regimes. Neglecting the second regime can lead to false estimate of achievable days of around 30% to reach SoH 90%. This might

Table II. Parameters of aging model shown in Fig. 4d.

Cell name	r_{pow}/*days*$^{-1}$	α/–	*Threshold*/*days*	*B*/–	r_{lin}/*days*$^{-1}$
4 °C *a*	0.0091	0.575	—	—	—
4 °C *b*	0.0111	0.495	—	—	—
19 °C *a*	0.0102	0.476	65.645	0.988	−0.0009
25 °C *a*	0.0074	0.583	50.007	0.988	−0.0013
25 °C *b*	0.0080	0.560	49.382	0.986	−0.0013
40 °C *a*	0.0044	0.812	28.418	1.031	−0.0035
45 °C *a*	0.0053	0.794	16.703	1.039	−0.0054
48 °C *a*	0.0037	0.970	21.641	1.094	−0.0077

become even more challenging when thermal inhomogeneities[19] and transients[19,80] are included.

Acknowledgments

L.C., M.S. and T.W. gratefully acknowledges the funding and support by the German Research Foundation (DFG) within the research training group SiMET under the project number 281041241/GRK2218. Also, the authors would like to thank Sabrina Herberger at TVT at KIT for support in test setup, Annette Schucker at IAM-ET at KIT for conducting EDX and XRD measurements on the BoL cell, Elisabeth Eiche at AGW at KIT for conducting ICP-OES measurements on the negative electrode covering layer and Volker Zibat at LEM at KIT for conducting SEM-EDX measurements. Many thanks also to Philipp Dechent at University of Oxford for the valuable discussions and thorough proof-read.

ORCID

L. Cloos https://orcid.org/0009-0006-1001-2891
M. Schiffler https://orcid.org/0009-0006-4606-102X
A. Weber https://orcid.org/0000-0003-1744-3732

References

1. J. Gorzelany, (2022), By The Numbers: Comparing Electric Car Warranties https://www.forbes.com/sites/jimgorzelany/2022/10/31/by-the-numbers-comparing-electric-car-warranties/.
2. M. S. Hosen, J. Jaguemont, J. van Mierlo, and M. Berecibar, *I. Science*, **24**, 102060 (2021).
3. M. Ecker, J. B. Gerschler, J. Vogel, S. Käbitz, F. Hust, P. Dechent, and D. U. Sauer, *J. Power Sources*, **215**, 248 (2012).
4. T. Gewald, A. Candussio, L. Wildfeuer, D. Lehmkuhl, A. Hahn, and M. Lienkamp, *Batteries*, **6**, 6 (2020).
5. T. Waldmann, B.-I. Hogg, and M. Wohlfahrt-Mehrens, *J. Power Sources*, **384**, 107 (2018).
6. P. M. Attia et al., *J. Electrochem. Soc.*, **169**, 60517 (2022).
7. B. E. Deal and A. S. Grove, *J. Appl. Phys.*, **36**, 3770 (1965).
8. R. Wright et al., *J. Power Sources*, **110**, 445 (2002).
9. J. Wang, J. Purewal, P. Liu, J. Hicks-Garner, S. Soukazian, E. Sherman, A. Sorenson, L. Vu, H. Tataria, and M. W. Verbrugge, *J. Power Sources*, **269**, 937 (2014).
10. P. M. Attia, W. C. Chueh, and S. J. Harris, *J. Electrochem. Soc.*, **167**, 090535 (2020).
11. L. von Kolzenberg, A. Latz, and B. Horstmann, *Chem. Sus. Chem.*, **13**, 3901 (2020).
12. I. Bloom et al., *J. Power Sources*, **101**, 238 (2001).
13. L. Lam and P. Bauer, *IEEE Trans. Power Electron.*, **28**, 5910 (2013).
14. M. Ecker, N. Nieto, S. Käbitz, J. Schmalstieg, H. Blanke, A. Warnecke, and D. U. Sauer, *J. Power Sources*, **248**, 839 (2014).
15. L. von Kolzenberg, A. Latz, and B. Horstmann, *Batteries & Supercaps*, **5**, e202100216 (2022).
16. S. F. Schuster, T. Bach, E. Fleder, J. Müller, M. Brand, G. Sextl, and A. Jossen, *Journal of Energy Storage*, **1**, 44 (2015).
17. M. Dubarry, C. Truchot, B. Y. Liaw, K. Gering, S. Sazhin, D. Jamison, and C. Michelbacher, *J. Power Sources*, **196**, 10336 (2011).
18. T. Waldmann, M. Wilka, M. Kasper, M. Fleischhammer, and M. Wohlfahrt-Mehrens, *J. Power Sources*, **262**, 129 (2014).
19. D. Werner, S. Paarmann, A. Wiebelt, and T. Wetzel, *Batteries*, **6**, 12 (2020).
20. S. Arrhenius, *Z. Physik. Chem.*, **4**, 226 (1889).
21. M. Broussely, S. Herreyre, P. Biensan, P. Kasztejna, K. Nechev, and R. Staniewicz, *J. Power Sources*, **97-98**, 13 (2001).
22. B. Y. Liaw, E. Roth, R. G. Jungst, G. Nagasubramanian, H. L. Case, and D. H. Doughty, *J. Power Sources*, **119-121**, 874 (2003).
23. X.-G. Yang and C.-Y. Wang, *J. Power Sources*, **402**, 489 (2018).
24. Y. Du, S. Shironita, E. Hosono, D. Asakura, Y. Sone, and M. Umeda, *J. Power Sources*, **556**, 232513 (2023).
25. G. Kucinskis, M. Bozorgchenani, M. Feinauer, M. Kasper, M. Wohlfahrt-Mehrens, and T. Waldmann, *J. Power Sources*, **549**, 232129 (2022).
26. M. Bozorgchenani, G. Kucinskis, M. Wohlfahrt-Mehrens, and T. Waldmann, *J. Electrochem. Soc.*, **169**, 030509 (2022).
27. Y. Preger, H. M. Barkholtz, A. Fresquez, D. L. Campbell, B. W. Juba, J. Romàn-Kustas, S. R. Ferreira, and B. Chalamala, *J. Electrochem. Soc.*, **167**, 120532 (2020).
28. M. Dubarry, C. Truchot, and B. Y. Liaw, *J. Power Sources*, **219**, 204 (2012).
29. K. Smith, A. Saxon, M. Keyser, B. Lundstrom, Z. Cao, and A. Roc, *2017 American Control Conference (ACC)* 4062 (IEEE) (2017).
30. M. Feinauer, M. Wohlfahrt-Mehrens, M. Hölzle, and T. Waldmann, *J. Power Sources*, **594**, 233948 (2024).
31. I. Bloom, A. N. Jansen, D. P. Abraham, J. Knuth, S. A. Jones, V. S. Battaglia, and G. L. Henriksen, *J. Power Sources*, **139**, 295 (2005).
32. T. Waldmann, G. Bisle, B.-I. Hogg, S. Stumpp, M. A. Danzer, M. Kasper, P. Axmann, and M. Wohlfahrt-Mehrens, *J. Electrochem. Soc.*, **162**, A921 (2015).
33. J. Schmitt, M. Schindler, A. Oberbauer, and A. Jossen, *J. Power Sources*, **532**, 231296 (2022).
34. V. W. Hu and D. T. Schwartz, *J. Electrochem. Soc.*, **169**, 030539 (2022).
35. D. W. Bacon and D. G. Watts, *Biometrika*, **58**, 525 (1971).
36. P. Fermín-Cueto, E. McTurk, M. Allerhand, E. Medina-Lopez, M. F. Anjos, J. Sylvester, and G. dos Reis, *Energy and AI*, **1**, 100006 (2020).
37. C. Strange, S. Li, R. Gilchrist, and G. dos Reis, *Energies*, **14**, 1206 (2021).
38. A. Cordoba-Arenas, S. Onori, Y. Guezennec, and G. Rizzoni, *J. Power Sources*, **278**, 473 (2015).
39. M. Fleckenstein, O. Bohlen, and B. Bäker, *WEVJ*, **5**, 322 (2012).
40. J. Purewal, J. Wang, J. Graetz, S. Soukiazian, H. Tataria, and M. W. Verbrugge, *J. Power Sources*, **272**, 1154 (2014).
41. D. A. Stevens, R. Y. Ying, R. Fathi, J. N. Reimers, J. E. Harlow, and J. R. Dahn, *J. Electrochem. Soc.*, **161**, A1364 (2014).
42. G. Kovachev, C. Ellersdorfer, G. Gstrein, I. Hanzu, H. M. R. Wilkening, T. Werling, F. Schauwecker, and W. Sinz, *E. Transportation*, **6**, 100087 (2020).
43. X.-G. Yang, Y. Leng, G. Zhang, S. Ge, and C.-Y. Wang, *J. Power Sources*, **360**, 28 (2017).
44. D. Anseán, M. Dubarry, A. Devie, B. Y. Liaw, V. M. García, J. C. Viera, and M. González, *J. Power Sources*, **356**, 36 (2017).
45. M. Dubarry and B. Y. Liaw, *J. Power Sources*, **194**, 541 (2009).
46. J. Sieg, M. Storch, J. Fath, A. Nuhic, J. Bandlow, B. Spier, and D. U. Sauer, *Journal of Energy Storage*, **30**, 101582 (2020).
47. A. J. Smith, P. Svens, M. Varini, G. Lindbergh, and R. W. Lindström, *J. Electrochem. Soc.*, **168**, 110530 (2021).
48. M. Tang, P. Albertus, and J. Newman, *J. Electrochem. Soc.*, **156**, A390 (2009).
49. F. Grimsmann, T. Gerbert, F. Brauchle, A. Gruhle, J. Parisi, and M. Knipper, *Journal of Energy Storage*, **15**, 17 (2018).
50. M. Storch, J. P. Fath, J. Sieg, D. Vrankovic, C. Krupp, B. Spier, and R. Riedel, *Journal of Energy Storage*, **41**, 102887 (2021).
51. Y. Zhu et al., *Nat. Commun.*, **10**, 2067 (2019).
52. P. Bai, J. Guo, M. Wang, A. Kushima, L. Su, J. Li, F. R. Brushett, and M. Z. Bazant, *Joule*, **2**, 2434 (2018).
53. C.-J. Ko, C.-H. Chen, and K.-C. Chen, *J. Power Sources*, **563**, 232779 (2023).
54. S. Paarmann, K. Schuld, and T. Wetzel, *Energy Tech.*, **10**, 2200384 (2022).
55. I. Yoshimatsu, T. Hirai, and J. Yamaki, *J. Electrochem. Soc.*, **135**, 2422 (1988).
56. N. M. Jobst, G. Gabrielli, P. Axmann, M. Hölzle, and M. Wohlfahrt-Mehrens, *J. Electrochem. Soc.*, **168**, 070550 (2021).
57. Z. Zhang et al., *Matter*, **4**, 302 (2021).
58. M. Varini, J. Y. Ko, P. Svens, U. Mattinen, M. Klett, H. Ekström, and G. Lindbergh, *Journal of Energy Storage*, **31**, 101616 (2020).
59. W. Li, X. Liu, Q. Xie, Y. You, M. Chi, and A. Manthiram, *Chem. Mater.*, **32**, 7796 (2020).
60. R. Jung, P. Strobl, F. Maglia, C. Stinner, and H. A. Gasteiger, *J. Electrochem. Soc.*, **165**, A2869 (2018).
61. M. S. D. Darma, M. Lang, K. Kleiner, L. Mereacre, V. Liebau, F. Fauth, T. Bergfeldt, and H. Ehrenberg, *J. Power Sources*, **327**, 714 (2016).
62. M. Lang, M. S. D. Darma, K. Kleiner, L. Riekehr, L. Mereacre, M. Ávila Pérez, V. Liebau, and H. Ehrenberg, *J. Power Sources*, **326**, 397 (2016).
63. P. Yan, J. Zheng, M. Gu, J. Xiao, J.-G. Zhang, and C.-M. Wang, *Nat. Commun.*, **8**, 14101 (2017).
64. M. Dubarry, C. Truchot, A. Devie, B. Y. Liaw, K. Gering, S. Sazhin, D. Jamison, and C. Michelbacher, *J. Electrochem. Soc.*, **162**, A1787 (2015).
65. E. Peled, *J. Electrochem. Soc.*, **126**, 2047 (1979).
66. A. Blyr, C. Sigala, G. Amatucci, D. Guyomard, Y. Chabre, and J.-M. Tarascon, *J. Electrochem. Soc.*, **145**, 194 (1998).
67. S. K. Martha et al., *J. Power Sources*, **189**, 288 (2009).
68. H. Tsunekawa, A. S. Tanimoto, R. Marubayashi, M. Fujita, K. Kifune, and M. Sano, *J. Electrochem. Soc.*, **149**, A1326 (2002).
69. G. Amatucci, A. Du Pasquier, A. Blyr, T. Zheng, and J.-M. Tarascon, *Electrochim. Acta*, **45**, 255 (1999).
70. P. Yang, J. Zheng, S. Kuppan, Q. Li, D. Lv, J. Xiao, G. Chen, J.-G. Zhang, and C.-M. Wang, *Chem. Mater.*, **27**, 7447 (2015).
71. M. Ecker, P. Shafiei Sabet, and D. U. Sauer, *Appl. Energy*, **206**, 934 (2017).
72. J. A. Gilbert, I. A. Shkrob, and D. P. Abraham, *J. Electrochem. Soc.*, **164**, A389 (2017).
73. K. Edström, T. Gustafsson, and J. O. Thomas, *Electrochim. Acta*, **50**, 397 (2004).
74. C. Zhan, J. Lu, A. Jeremy Kropf, T. Wu, A. N. Jansen, Y.-K. Sun, X. Qiu, and K. Amine, *Nat. Commun.*, **4**, 2437 (2013).
75. K. Amine, J. Liu, S. Kang, I. Belharouak, Y. Hyung, D. Vissers, and G. Henriksen, *J. Power Sources*, **129**, 14 (2004).
76. A. Nitzan and M. A. Ratner, *J. Phys. Chem.*, **98**, 1765 (1994).
77. B.-R. Chen, C. M. Walker, S. Kim, M. R. Kunz, T. R. Tanim, and E. J. Dufek, *Joule*, **6**, 2776 (2022).
78. I. Baghdadi, O. Briat, J.-Y. Delétage, P. Gyan, and J.-M. Vinassa, *J. Power Sources*, **325**, 273 (2016).
79. T. Waldmann, N. Ghanbari, M. Kasper, and M. Wohlfahrt-Mehrens, *J. Electrochem. Soc.*, **162**, A1500 (2015).
80. L. Cloos, O. Queisser, A. Chahbaz, S. Paarmann, D. U. Sauer, and T. Wetzel, *Batteries & Supercaps*, **7**, e202300445 (2024).